

# *Patient-specific isogeometric structural analysis of aortic valve closure*

S. Morganti<sup>a\*</sup>, F. Auricchio<sup>b</sup>, D. Benson<sup>c</sup>, F.I. Gambarin<sup>d</sup>, S. Hartmann<sup>e</sup>, T.J.R. Hughes<sup>f</sup>, A. Reali<sup>b</sup>

<sup>a</sup> Dipartimento di Ingegneria Industriale e dell'Informazione, Università degli Studi di Pavia,  
via Ferrata 1, 27100 Pavia, Italy

<sup>b</sup> Dipartimento di Ingegneria Civile e Architettura, Università degli Studi di Pavia,  
via Ferrata 1, 27100 Pavia, Italy

<sup>c</sup> Department of Structural Engineering, University of California, 9500 Gilman Drive, La Jolla, CA 92093, USA

<sup>d</sup> Cardiology Unit, S. Pio X Hospital, Opera S. Camillo Foundation, via Nava 31, 20159 Milano, Italy

<sup>e</sup> Dynamore GmbH, Industriestr. 2, D-70565 Stuttgart, Germany

<sup>f</sup> The Institute of Computational Engineering and Sciences (ICES), University of Texas at Austin, 201 East 24th Street, 1 University Station C0200, Austin, TX 78712, USA

## Abstract

We investigate the use of Isogeometric Analysis for the model construction and simulation of aortic valve closure. We obtain converged results and compare with benchmark finite element analysis. We find that Isogeometric Analysis is capable of attaining the same accuracy with models consisting of two orders of magnitude fewer nodes than finite element models; analogous savings are observed also in terms of analysis time. Model construction and mesh refinement are likewise performed more efficiently with Isogeometric Analysis.

## 1 Introduction

The aortic valve regulates blood flow from the left ventricle to the aorta. Its crucial physiologic function and complex anatomy have motivated biomedical engineers to try to understand and explain aortic valve behavior using computer models. Even though the first aortic valve models date back to the 70s [1, 2, 3, 4], the complex physiological and pathological behavior of aortic valves have generated great contemporary interest [5, 6, 7, 8, 9]. In fact, the increase of population average age and of life expectancy makes heart valve disease and degeneration serious and constantly growing public-health problems, requiring appropriate resources to improve diagnosis and treatment [10].

The application of modern computational techniques for heart valve modeling represents a challenging research activity that may lead to the development of diagnostic tools, therapeutic devices, innovative prostheses, and the prediction of surgical outcomes. The purpose of the present work is to develop simple and accurate modeling and analysis procedures for the simulation of aortic valves. To accomplish this goal, we adopt isogeometric analysis (IgA) that may have significant advantages over other modelling and analysis procedures.

---

\*Corresponding author. Email: simone.morganti@unipv.it

Introduced in 2005 [11], IgA employs typical functions from Computer Aided Design (such as, e.g., NURBS) for describing both geometry and field variables in an isoparametric fashion [12, 13, 14]. This leads to precise geometrical representations, typically exhibiting superior accuracy per degree of freedom with respect to finite elements [15, 16, 17, 12, 18]. Since accurate results deriving from very precise geometrical descriptions and reduced computational times are key ingredients of computer-based simulations, especially in the field of predictive biomedicine, in this paper we aim at showing the suitability of isogeometric techniques for the simulation of aortic valves. In particular, starting from contrast-enhanced Computed Tomography Angiography (CTA) images in Dicom format, we obtain a stereolithographic (STL) representation of the aortic root, which is used as the target object to generate an isogeometric patient-specific model through a mapping procedure. Aortic leaflets, not visible with CTA, are constructed by integrating CTA data and ultrasound information, completing an aortic valve multi-patch structure. The diastolic behavior (corresponding to valve closure) of the aortic valve is calculated with isogeometric analysis. The “image-to-analysis” approach developed to perform patient-specific IgA of the aortic valve is sketched in the flowchart of Figure 1 and compared to the corresponding one for finite element analysis (FEA).

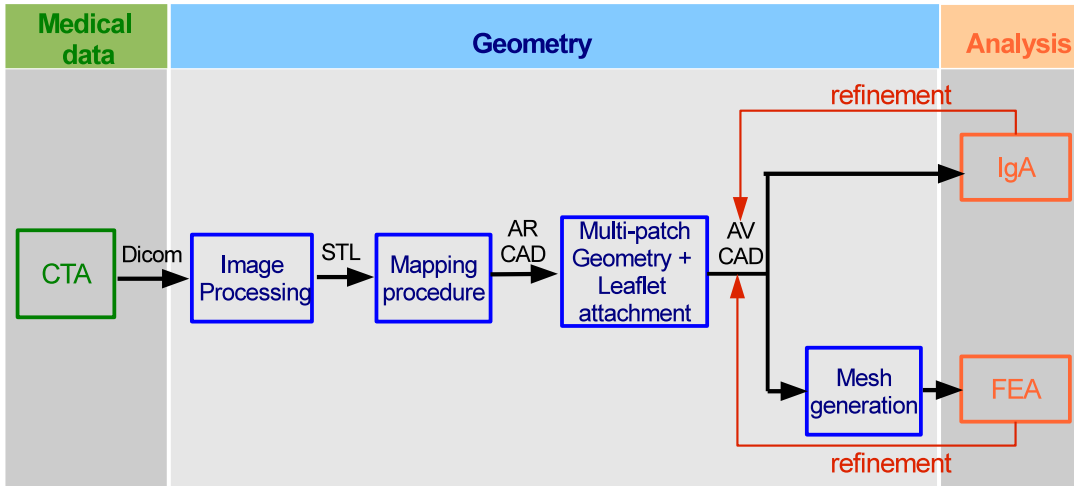


Figure 1: From medical images to analysis: Flowchart summary followed to perform a computational analysis of patient-specific aortic valve closure using IgA (top branch) or FEA (bottom branch).

AR stands for aortic root, AV stands for aortic valve.

The procedure to obtain a CAD representation of the aortic valve with the leaflets is the same in the two cases. However, following an IgA approach, the CAD representation is already an analysis-suitable model, while for finite elements a mesh generation step, that can be time consuming for complex geometries, is required. Additionally, when mesh refinement is necessary, with IgA a simple and inexpensive knot insertion (or degree elevation) operation at the CAD level is all that is required, while for finite elements a completely new mesh generation step has to be performed.

The paper is structured as follows: in Section 2, after presenting some basic concepts of IgA, we propose the approach to construct patient-specific geometries from medical images; in Section 3 we describe the isogeometric model of the aortic valve; and in Section 4 we present

the simulation results. We draw conclusions in Section 5.

## 2 B-splines, NURBS and patient-specific modeling

Our procedure to obtain patient-specific surfaces is based on Non-Uniform Rational B-Splines (NURBS), which represent the dominant technology for design and geometric representation in industry. We also use NURBS for the approximation of field variables. In this section we give a very brief introduction to NURBS (details can be found in the book by Piegl and Tiller [19]) and to their use to construct an analysis-suitable geometrical model of the aortic valve starting from CTA images.

### 2.1 Basic concepts of B-splines and NURBS

NURBS are obtained from B-splines, which are piecewise polynomial curves composed of linear combinations of B-spline basis functions. A brief description of B-splines is therefore presented first.

B-spline basis functions are constructed from a set of parametric coordinates, collected in a *knot vector*, i.e., a non-decreasing sequence of real numbers:  $\Xi = \{\xi_1, \dots, \xi_{n+p+1}\}$ , where  $p$  is the polynomial degree and  $n$  is the number of basis functions determined by the knots. The interval:  $[\xi_1, \xi_{n+p+1}]$  is called a *patch*. A knot vector is called *open* if the first and last knot have multiplicity  $p + 1$ . In this case, the basis is interpolatory at the boundary points of the patch. The  $i$ -th basis function of order  $p$  is defined recursively, starting from the piecewise constants ( $p = 0$ ) according to the Cox-de-Boor recursion formula. For  $p = 1, 2, 3, \dots$  the basis functions are defined by:

$$N_i^p(\xi) = \frac{\xi - \xi_i}{\xi_{i+p} - \xi_i} N_i^{p-1}(\xi) + \frac{\xi_{i+p+1} - \xi}{\xi_{i+p+1} - \xi_{i+1}} N_{i+1}^{p-1}(\xi), \quad (1)$$

while for  $p = 0$ :

$$N_i^0(\xi) = \begin{cases} 1 & \text{if } \xi_i \leq \xi < \xi_{i+1}, \\ 0 & \text{otherwise.} \end{cases} \quad (2)$$

Further details may be found in [12].

A linear combination of the basis functions results in a B-spline curve:

$$\mathbf{C}(\xi) = \sum_{i=1}^n N_i^p(\xi) \mathbf{B}_i \quad 0 \leq \xi \leq 1, \quad (3)$$

where  $\mathbf{B}_i$  are the so-called *control points*.

In Figure 2(a) quadratic basis functions determined by the open knot vector  $\Xi = \{0, 0, 0, 1, 2, 3, 3, 4, 4, 4\}$  are shown, and in Figure 2(b) an example of a B-spline curve constructed using this basis is shown along with its control polygon (i.e., the polygon obtained by linear interpolation of the control points).

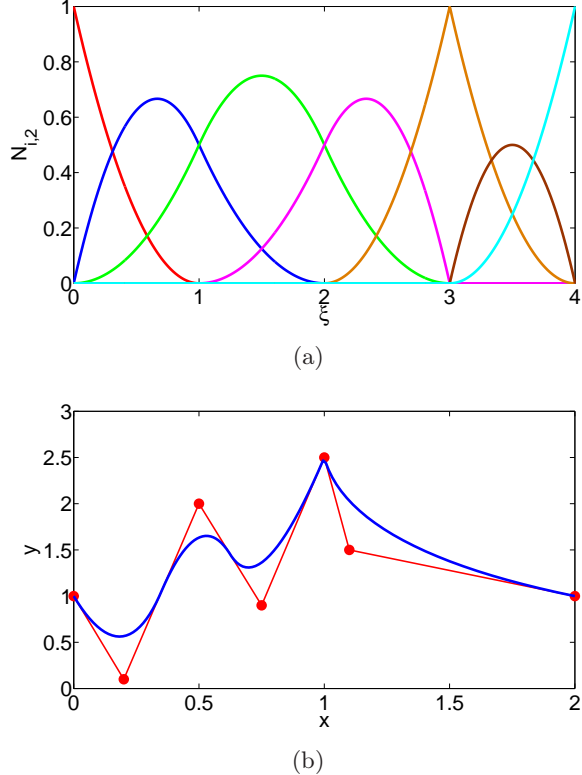


Figure 2: Example of a B-spline basis functions and curve. (a) Quadratic B-spline basis functions formed from the open knot vector  $\Xi = \{0, 0, 0, 1, 2, 3, 3, 4, 4, 4\}$ . (b) B-spline curve and control polygon. Since an open knot vector is chosen, the curve is interpolatory at the first and last control points and, due to the  $p$ -multiplicity of a knot, the curve is interpolatory also at one interior control point.

B-spline surfaces are obtained by the tensor product of B-spline curves. Given a net of control points  $\mathbf{B}_{i,j}$ , two knot-vectors  $\Xi = \{\xi_1, \dots, \xi_{n+p+1}\}$  and  $\mathcal{H} = \{\eta_1, \dots, \eta_{m+q+1}\}$ , and two polynomial degrees  $p$  and  $q$ , a tensor-product B-spline surface is defined by:

$$\mathbf{S}(\xi, \eta) = \sum_{i=1}^n \sum_{j=1}^m N_i^p(\xi) M_j^q(\eta) \mathbf{B}_{i,j}. \quad (4)$$

A NURBS entity in  $\mathbb{R}^d$  is obtained by the projective transformation of a B-spline entity in  $\mathbb{R}^{d+1}$ . Moving from B-splines to NURBS allows the *exact* representation of a wide range of objects that cannot be exactly represented by polynomials (e.g., conic sections like circles and ellipses).

A NURBS curve is a rational function given by:

$$\mathbf{C}(\xi) = \sum_{i=1}^n R_i^p(\xi) \mathbf{B}_i, \quad (5)$$

where the basis functions  $R_i^p$  are obtained from B-spline basis functions  $N_i^p$  as follows:

$$R_i^p(\xi) = \frac{N_i^p(\xi)w_i}{\sum_{\hat{i}=1}^n N_{\hat{i}}^p(\xi)w_{\hat{i}}},$$

being  $w_i$  the  $i$ -th weight. See [12] for further details.

A NURBS surface is then given by:

$$\mathbf{S}(\xi, \eta) = \sum_{i=1}^n \sum_{j=1}^m R_{i,j}^{p,q}(\xi, \eta) \mathbf{B}_{i,j}, \quad (6)$$

with:

$$R_{i,j}^{p,q}(\xi, \eta) = \frac{N_i(p\xi)M_j^q(\eta)w_{i,j}}{\sum_{\hat{i}=1}^n \sum_{\hat{j}=1}^m N_{\hat{i}}^p(\xi)M_{\hat{j}}^q(\eta)w_{\hat{i},\hat{j}}}. \quad (7)$$

## 2.2 Cardiovascular patient-specific geometrical modeling of the aortic valve

The aortic valve, one of the four heart valves, is located between the left ventricle and the aorta. Neglecting anatomical details, its two main parts are the aortic root and the aortic leaflets. The aortic root represents the connection between the aorta and the myocardium, and is made of three pouch-like dilatations, called Valsalva sinuses (red parts in Figure 3), while the aortic leaflets are semilunar flexible membranes which regulate blood flow by opening during systole and closing during diastole (light pink parts in Figure 3). Leaflets are named, in relation to the coronary arteries, left-coronary, right-coronary, and non-coronary leaflet. The non-coronary leaflet is typically larger in terms of area, perimeter, and attachment edge than the other two [20].

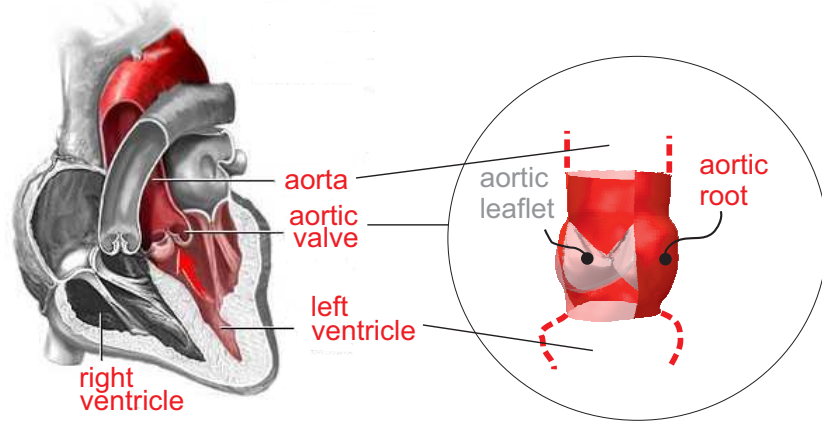


Figure 3: The aortic valve: Position and main structural components.

The aortic valve geometry can be relatively easily extracted from medical images. Computed Tomography Angiography (CTA) is routinely adopted for the diagnosis of aortic valve

pathologies and represents an efficient tool for aortic root reconstruction as a contrast agent is used to highlight the aortic lumen. Since the aortic leaflets are usually not visible with CTA, ultrasound measurements can be integrated with CTA data to allow a patient-specific geometrical reconstruction of the leaflets. In the following, the procedure to obtain a NURBS representation of both the aortic root and the leaflets from medical images is discussed.

### 2.2.1 Aortic root geometry

For the geometry reconstruction procedure, CTA images from a 29 year-old female patient with normal aortic valve morphology are utilized. Scan data are characterized by the following parameters: slice thickness = 0.6 mm; slice width  $\times$  height = 512  $\times$  512 pixels; pixel spacing = 0.56 mm.

#### From medical images to an STL file

The freeware imaging software OsiriX [21] is used to process the imaging data. We first proceed with an automatic cropping and segmentation procedure and then manually finish the extraction of the aortic root (see Figures 4(a) and (b)). This is then exported as an STL representation, i.e., a very fine triangular mesh, not directly useful for analysis (see Figure 4(c)).

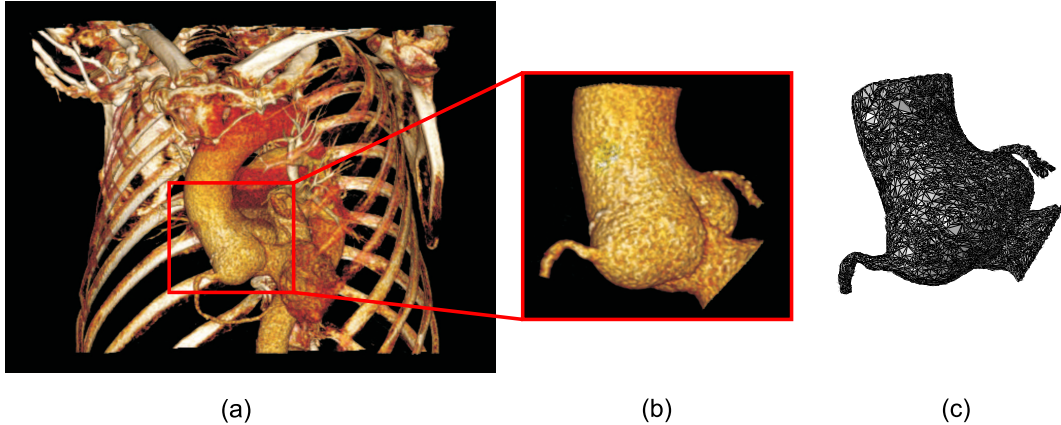


Figure 4: From CTA to STL file: (a) Primary 3D reconstruction obtained using OsiriX; (b) 3D specific reconstruction of the aortic root after cropping and segmentation procedures; (c) STL representation of the extracted region of interest.

#### Mapping procedure

We propose a simple and fast procedure to map a basic primitive NURBS geometry (e.g., a cylinder) onto a target image-based surface given by the STL file. The proposed mapping procedure determines the best location of the control points to represent the target surface evaluated at a set of  $N_s$  sampling points (with  $N_s$  greater than the total number of control points,  $N_{cp} = n \times m$ ) in a least-squares sense. The idea is illustrated by mapping a NURBS cylinder onto the STL mesh of an aortic root. The cylinder surface is obtained by sweeping a circle over a vertical distance  $h$ . One way to construct the NURBS circle to be swept is by

piecing together three arcs of  $120^\circ$  using a seven-point triangular control polygon [19]; this is not the only option, but seems to be the most convenient one, given the root morphology (naturally divided into three sinuses).

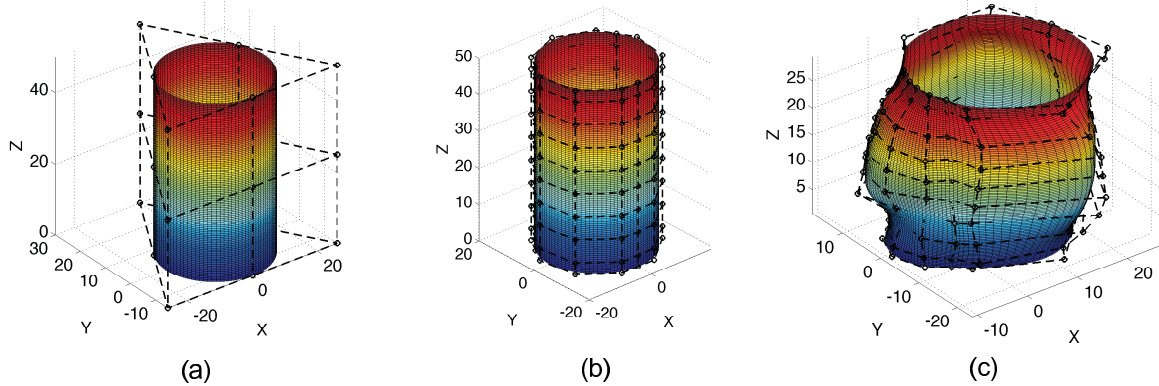


Figure 5: Mapping procedure: (a) Control mesh of a seven-point triangle-based NURBS cylinder ( $radius = 15$  mm,  $h = 50$  mm); (b) Result of the knot insertion procedure (120 control points); (c) Resulting NURBS surface of the patient-specific aortic root and its control mesh.

In Figure 5(a) a NURBS cylinder is shown with the associated control polygon. In order to get a better reproduction of the aortic root, we first refine the mesh by knot insertion [11]. The original knot vectors  $\Xi = \{\xi_1, \xi_2, \dots, \xi_{n+p+1}\}$  and  $\mathcal{H} = \{\eta_1, \eta_2, \dots, \eta_{m+q+1}\}$  are extended to  $\bar{\Xi} = \{\bar{\xi}_1 = \xi_1, \bar{\xi}_2, \dots, \bar{\xi}_{n+\bar{n}+p+1} = \xi_{n+p+1}\}$  and  $\bar{\mathcal{H}} = \{\bar{\eta}_1 = \eta_1, \bar{\eta}_2, \dots, \bar{\eta}_{m+\bar{m}+q+1} = \eta_{m+q+1}\}$  such that  $\Xi \subset \bar{\Xi}$  and  $\mathcal{H} \subset \bar{\mathcal{H}}$  [12]. In Figure 5(b) the result of the knot insertion operation is shown. Finally, a least-squares mapping operation is performed and the result shown in Figure 5(c) is obtained.

### 2.2.2 Aortic leaflet geometry

Once we have a patient-specific aortic root constructed from CTA records, as indicated in the previous section, we still have to complete the aortic valve anatomy by including the aortic leaflets. Unfortunately, CTA images do not usually allow leaflet reconstruction, but it is possible to highlight the segments where they are attached to the aortic root, as shown in Figure 6(a). The leaflet free margin length (green curve in Figure 6(b)) can be instead measured from ultrasound short-axis projection. The union of such lines allows leaflet edge reconstruction. It is then easy to generate the leaflet NURBS surfaces exploiting CAD softwares (see Figure 6(c)); we use Rhinoceros, version 4.0.

### 2.2.3 Aortic valve geometry: attachment of the leaflets to the aortic root

The aortic valve geometry is obtained by coupling the leaflet and root models. We partition the aortic root surface to generate  $C^0$  lines corresponding to the leaflet lines of attachment. We then require the same parameterizations along corresponding lines on the root and on the leaflets, and merge coincident control points to obtain a conforming multi-patch geometry, given by the assembly of all patches shown in Figure 7.

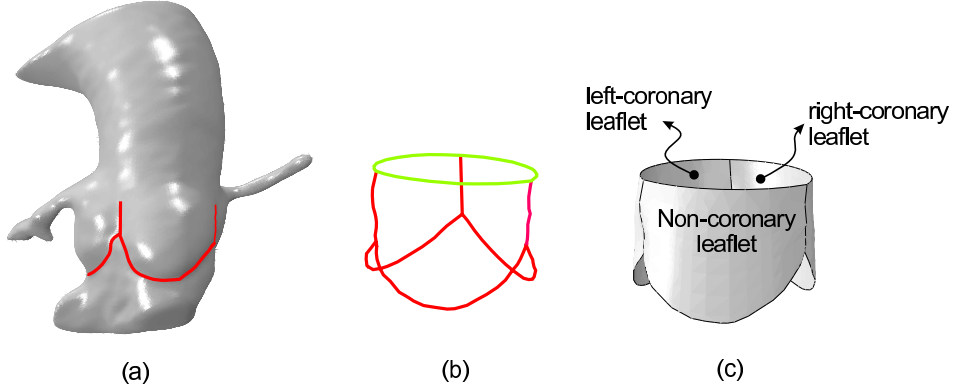


Figure 6: Procedure to create aortic leaflet model: (a) The lines of attachment can be identified on the aortic lumen reconstruction from CTA images (red lines); (b) Three circular arcs (green lines) are drawn to complete the leaflet model based on ultrasound measurements; (c) NURBS surfaces are defined exploiting CAD software capabilities.

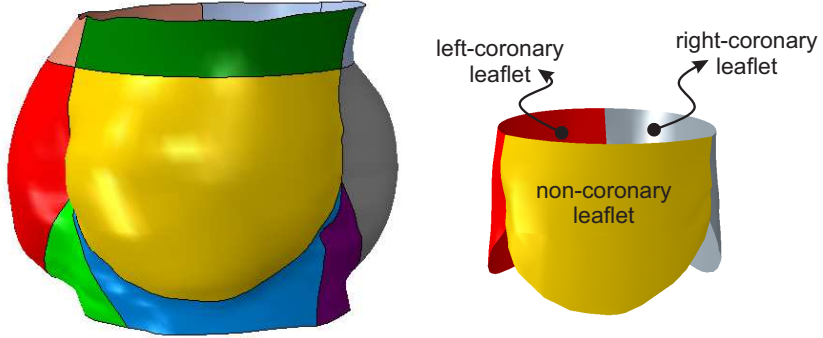


Figure 7: Multi-patch aortic valve geometry: (a) The aortic root is subdivided into nine NURBS patches; (b) Each leaflet represents a single patch.

### 3 Aortic valve structural analysis

The obtained aortic valve geometry consists of 12 biquadratic surface patches (nine root patches and three leaflet patches). We refine meshes through knot insertion. Three meshes are constructed, a coarse mesh of 762 control points, a medium one of 2890 control points, and a fine mesh of 9396 control points (see Figure 8).

The aortic root is modeled with a Reissner-Mindlin shell formulation [22] utilising six degrees of freedom per node, while for the aortic leaflets a rotation-free Kirchhoff-Love shell formulation [23] with three degrees of freedom per node is used. This choice is justified by the significant differences in thickness and flexibility of the root and the leaflets. Specifically, a thickness of 1.5 mm has been considered for the root and 0.25 mm for the leaflets, according to physiological values [24]. All calculations are performed with LS-DYNA [25]. Explicit time stepping is used to obtain the equilibrium configuration.

Following [6, 26], we adopt a nearly-incompressible isotropic hyperelastic Mooney-Rivlin constitutive law based on the following strain energy function:

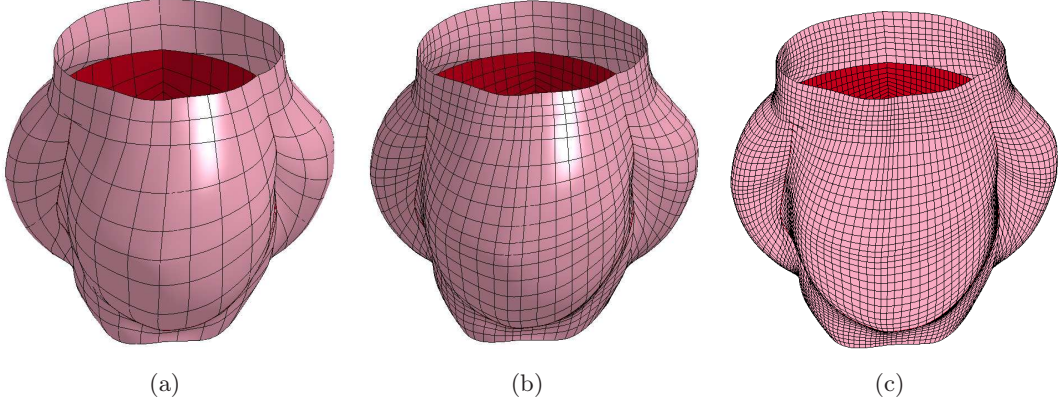


Figure 8: NURBS meshes (knot-spans) for a patient-specific aortic root (pink) and leaflets (red): (a) Coarse mesh (762 control points); (b) Medium mesh (2890 control points); (c) Fine mesh (9396 control points).

$$W = A(I_1 - 3) + B(I_2 - 3) + C\left(\frac{1}{I_3^2} - 1\right) + D(I_3 - 1)^2, \quad (8)$$

where  $A$  and  $B$  are material parameters taken as  $A = 0.5516$  MPa and  $B = 0.1379$  MPa, while  $C$  and  $D$  are defined as:

$$C = \frac{1}{2}A + B, \quad (9)$$

$$D = \frac{A(5\nu - 2) + B(11\nu - 5)}{2(1 - 2\nu)}, \quad (10)$$

where  $\nu$  is the Poisson's ratio, assumed equal to 0.495.

A uniform pressure load of 0.01 MPa is applied to the aortic leaflets to reproduce diastolic behavior, while the control points belonging to both the top and the bottom of the aortic root model are confined to the plane of their original configuration. Finally, a standard single surface contact algorithm [25] is used to model the interactions among the three leaflets during valve closure.

## 4 Results

We present the numerical results obtained from an explicit nonlinear isogeometric analysis using the model described in the previous section. We compare results with those of a standard explicit nonlinear finite element analysis performed with the same software. Results are first presented for the coaptation length, a measure of how much the three aortic leaflets are in contact with each other at the end of diastole. The coaptation length is defined as the distance between the coaptation profile and the leaflet free margin. In Figure 9 the coaptation area (in red) is shown.

The coaptation length is a very significant medical parameter as it is directly associated with valve functionality and competence. If the leaflets are not properly coapting, a surgical

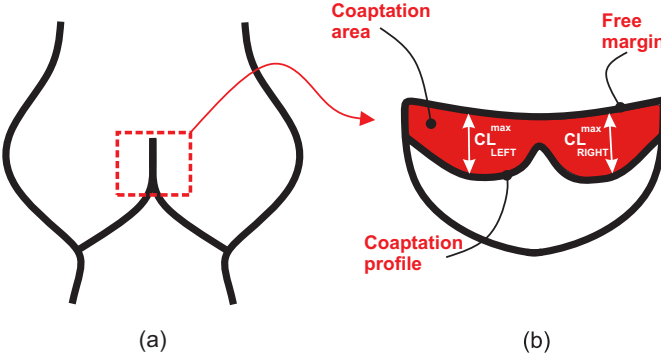


Figure 9: Cohesion area: (a) Longitudinal section of the aortic valve during diastole; (b) The cohesion area, the leaflet free margin, and the cohesion profile for one leaflet are labeled.

intervention is generally needed. Once surgery has been performed, success is also evaluated by measuring the post-operative coaptation length.

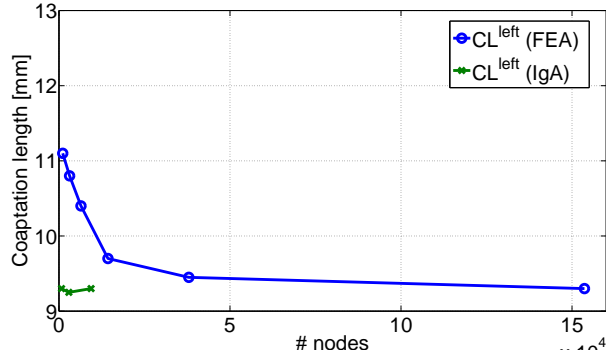
Table 1: Simulation results in terms of coaptation length for isogeometric and finite element analysis.

Analysis	# nodes	# DOF	Cohesion length	
			$CL_{left}^{max}$ [mm]	$CL_{right}^{max}$ [mm]
IgA	762	3708	9.30	9.40
	2890	19476	9.25	9.40
	9396	50496	9.30	9.35
FEA	1112	6672	11.1	12.8
	3117	18702	10.8	10.2
	6446	38676	10.4	9.80
	14329	85974	9.70	9.70
	37972	227832	9.45	9.50
	153646	921876	9.30	9.35

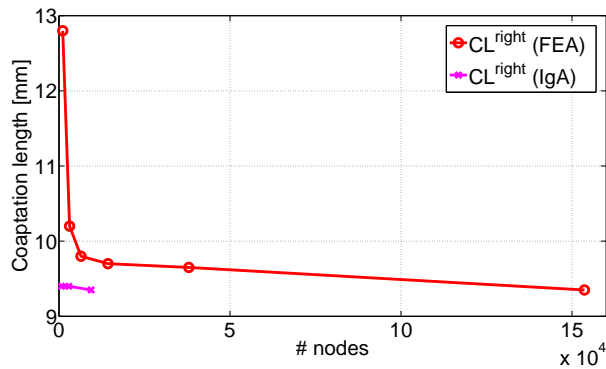
Isogeometric analysis results are compared with finite element simulations. For the finite element analyses, Belytschko-Tsay 4-node Reissner-Mindlin shells have been used to model the entire aortic valve. Table 1 reports the results in terms of coaptation length. Since control points in isogeometric analysis play the same role as nodes in finite element analysis, to simplify the terminology, we will refer to them as nodes. In Figure 10 the maximum coaptation lengths of the non-coronary leaflet are plotted versus the number of nodes.

Figure 11 shows the coaptation areas for the coarsest (already converged) isogeometric analysis and the second finest finite element analysis (which, on the basis of the results of Table 1 might be identified as nearly converged).

The following two observations are indications that the isogeometric analysis results more faithfully represent the physiological case than do the finite element results: (i) The coaptation length at the leaflet insertion in the aortic wall should be considerably smaller than the maximum coaptation length, due to the presence of the so-called interleaflet triangles, which



(a)



(b)

Figure 10: IgA vs FEA. Maximum coaptation length of the non-coronary leaflet as a function of the number of nodes: (a) Left side leaflet; (b) Right side leaflet.

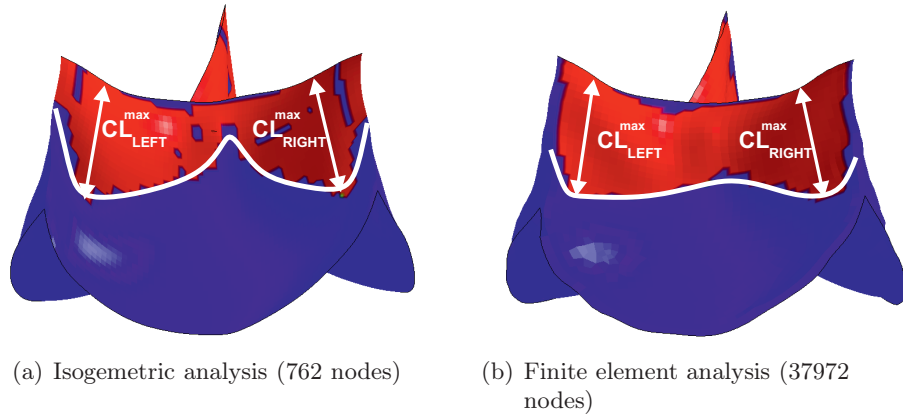


Figure 11: Results of physiologic valve closure: contact interface pressure highlighting the coaptation area of the non-coronary leaflet.

are triangular extensions of the left ventricle “bordered by insertion of the leaflets and of the leaflet attachments of the aortic sinuses at their base” [27]; (ii) Going from the leaflet insertion zone to the center of the valve, the slope of the coaptation profile should vary significantly in

correspondence with the Arantius's nodule at the center of the leaflet.

We have studied a number of CT images from different patients with healthy aortic valves (with at least partially visible leaflets), and we found out that the typical situation is the one reported in Figure 12, where the ratio  $\frac{CL_{attach}}{CL_{max}}$  is of order 60% and the ratio  $\frac{CL_{center}}{CL_{max}}$  is of order 25%. This clearly supports claims (i) and (ii), as well as the apparently more physiological closure result provided by IgA.

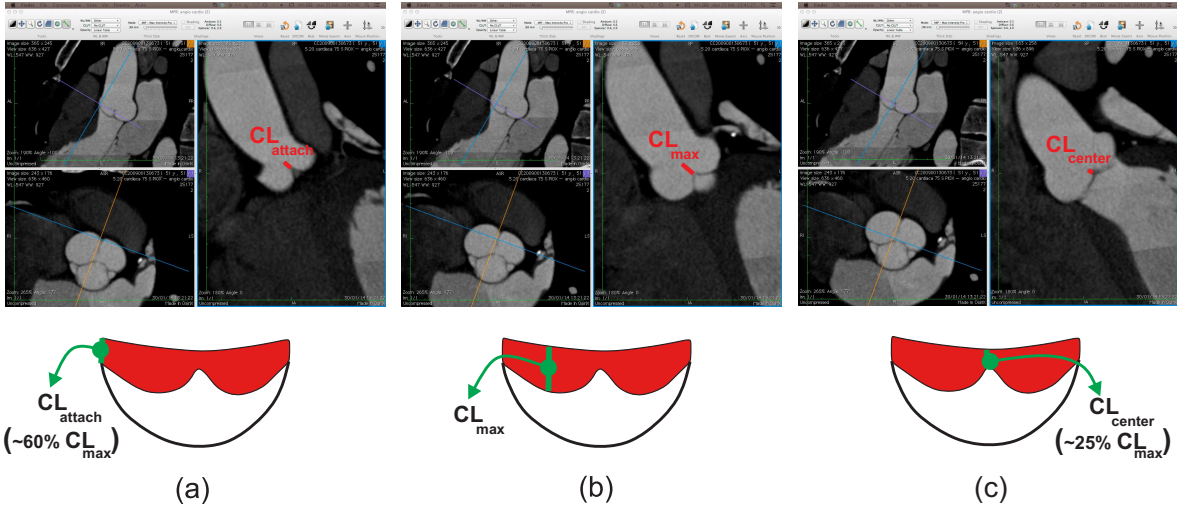


Figure 12: CT multi-planar reconstruction: (a) the coaptation length at the leaflet insertion in the aortic wall is highlighted and measured (60% of  $CL_{max}$ ); (b) the maximum coaptation length is highlighted and measured; (c) the coaptation length at the center of the aortic valve is highlighted and measured (25% of  $CL_{max}$ ).

Given the poor FEA results in terms of coaptation profile, we decided to further refine the finite element analysis seeking a more physiological result. Actually, the finest FEA mesh in Table 1 (i.e., the 153646 nodes mesh) provides a similar result to that obtained with IgA. This is represented in Figure 13 and proves that the second finest FEA mesh cannot be considered as converged.

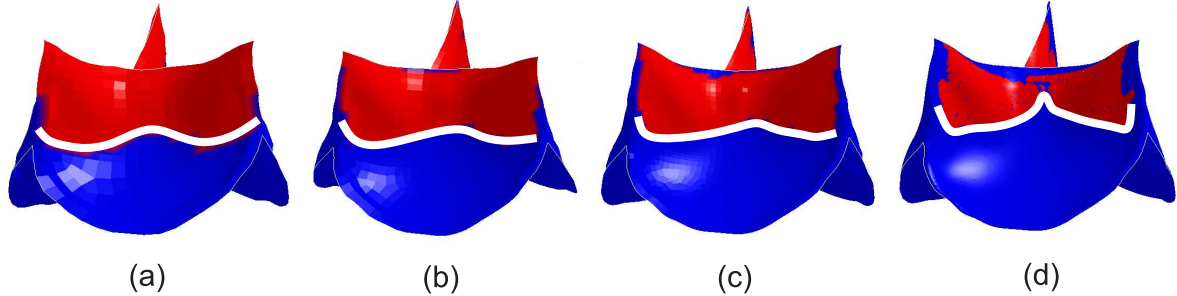


Figure 13: Finite element analysis results. The coaptation area is shown for four different meshes: (a) 6446 nodes; (b) 14329 nodes; (c) 37972 nodes; (d) 153646 nodes.

Instead, as shown in Figure 14, the coarsest IgA mesh (i.e., the 762 nodes mesh) provides

results which can be considered converged for practical purposes even in terms of coaptation profile.

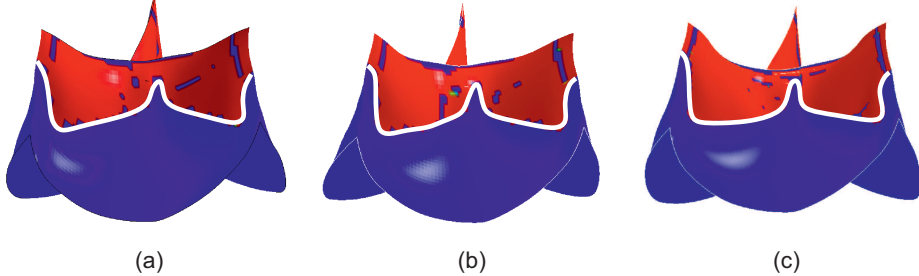


Figure 14: Isogeometric analysis results. The coaptation area is shown for three different meshes: (a) 762 nodes; (b) 2890 nodes; (c) 9396 nodes.

As can be seen from the comparison of Figures 13(d) and 14(a), converged isogeometric and finite element results appear to be in very good agreement. However, isogeometric analysis requires more than two orders of magnitude fewer nodes to capture the converged values. Even the coarsest isogeometric mesh seems to be sufficiently accurate for diagnostic purposes.

In addition to coaptation lengths and profiles, we also consider displacement and stress distributions to further validate our comparison between isogeometric and finite element analyses. In Figure 15, the displacement magnitude of the leaflets is shown for the coarsest isogeometric mesh and for the finest finite element mesh. The deformed configurations of the closed valve are in very good agreement and the displacement field is practically the same in both cases. Both Figures 15(a) and (b) show a smooth and physiologic diastolic configuration.

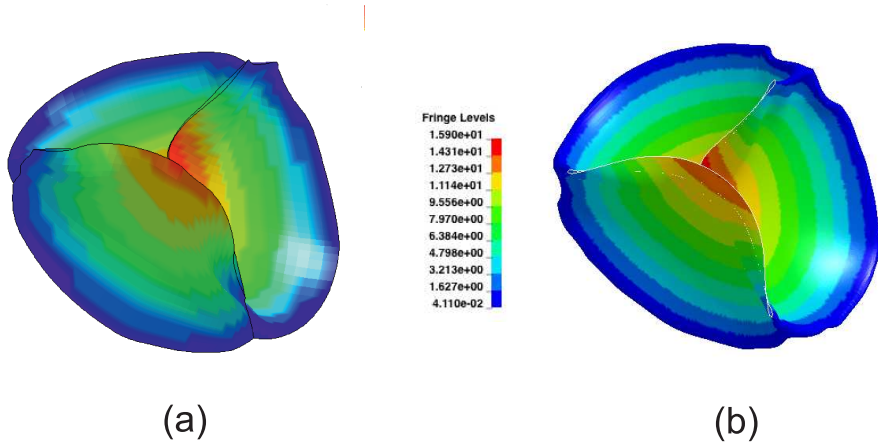


Figure 15: Resultant displacements: Detail of the leaflet model. (a) Isogeometric analysis of valve closure (762 nodes); (b) Finite element analysis of valve closure (153646 nodes).

In Figure 16, also the von Mises stress of the leaflets is shown for the coarsest isogeometric mesh and for the finest finite element mesh. Stress distribution on the aortic valve structure is of clinical interest because it is associated to failure phenomena [6, 28]: Localized stress concentration is in fact related to calcification and tissue degeneration [29]. Additionally, high stress values may potentially induce aortic valve remodeling and increased thickness [30],

which may lead to aortic tissue stiffening and, consequently, to the loss of physiologic pull-and-release function and to leaflet degeneration [31]. The stress patterns of the closed aortic valve resulting from the isogeometric and finite element analyses appear very similar: the aortic root has negligible stresses, the peak stress is at the top of the commissures (i.e., the vertical lines of leaflet attachment to the aortic root), and the stress distribution on the leaflet belly is quite uniform, around 0.3 MPa. The isogeometric simulation results seem to be somewhat closer to the physiologic case showing low stress values in proximity of the lines of leaflet attachment.

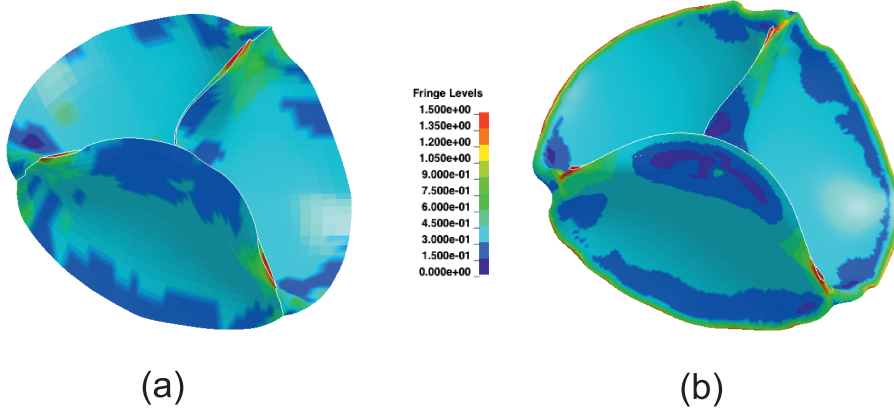


Figure 16: Von Mises stress pattern: Detail of the leaflet model. (a) Isogeometric analysis of valve closure (762 nodes); (b) Finite element analysis of valve closure (153646 nodes).

The comparison between isogeometric and finite element analyses shows a good agreement in terms of coaptation length, deformed valve configuration, and stress pattern. Moreover, IgA requires orders of magnitude fewer nodes with respect to finite elements to capture the converged solution.

Many issues need to be considered to fairly compare the efficiency of IgA and FEA (e.g., different shell models and approximation degrees for FEA and IgA, integration rules [32, 33], and solvers for IgA, etc.), however, it is interesting to provide our data for the two converged analyses, as reported in Table 2. The converged IgA is over 440 times faster than the converged FEA, taking about 1 hour of computational time versus about 23 full 24 hour days.

Table 2: Computational times for isogeometric and finite element analysis.

Analysis	# nodes	# cpus	time step	# increments	total analysis time
IgA	762	12	2.30e-07	4347490	<b>1h 15m</b>
FEA	153646	12	2.65e-08	37787314	<b>550h 23m</b>

Finally, it is also worth remarking that, using isogeometric analysis, it is possible to quite easily obtain accurate analysis-suitable meshes of patient-specific geometries and the refinement process can be done without the need to regenerate the computational model from the STL representation obtained from medical images, as is required with standard finite element analysis.

## 5 Conclusions

An isogeometric analysis approach has been proposed to model aortic valve closure, involving large deformations and contact of patient-specific geometries. Isogeometric analysis requires more than two orders of magnitude fewer nodes to capture converged solutions, and analogous savings have also been observed in terms of analysis time. Moreover, model construction and mesh refinement are much more efficiently performed, as highlighted by the “image-to-analysis” flow in Figure 1. This application clearly shows how isogeometric analysis can be regarded as a viable and efficient tool for the simulation of complex biomechanical problems, which are typically very demanding for standard finite elements in terms of geometry construction, accuracy, and computational cost.

## 6 Acknowledgements

This work is partially funded by the European Research Council through the Project no. 259229 entitled ‘ISOBIO: Isogeometric Methods for Biomechanics’, partially by MIUR through the PRIN Project no. 2010BFXRHS, and partially by the Cariplò/Regione Lombardia project ICardioCloud no. 2013-1779.

## References

- [1] R.E. Clark and G.A.M. Butterworth. Characterization of the mechanics of human aortic and mitral valve leaflets. *Surgical forum*, 22:134–136, 1971.
- [2] R.E. Clark. Stress-strain characteristics of fresh and frozen human aortic and mitral leaflets and chordae tendineae. *Journal of Thoracic and Cardiovascular Surgery*, 66:202–208, 1973.
- [3] P.L. Gould, A. Cataloglu, G. Dhatt, A. Chattophadyay, and R.E. Clark. Stress analysis of the human aortic valve. *Computers and structures*, 3:377–384, 1973.
- [4] P.L. Gould, A. Cataloglu, and R.E. Clark. Mathematical modelling of human aortic valve leaflets. *Applied Mathematical Modelling*, 1:33–36, 1976.
- [5] K.J. Grande, R.P. Cochran, P.G. Reinhall, and K.S. Kunzelman. Mechanisms of aortic valve incompetence: finite element modeling of Marfan syndrome. *The Journal of Thoracic and Cardiovascular Surgery*, 122:946–954, 2001.
- [6] A. Ranga, O. Bouchot, R. Mongrain, P. Ugolini, and R. Cartier. Computational simulations of the aortic valve validated by imaging data: evaluation of valve-sparing techniques. *Interactive CardioVascular and Thoracic Surgery*, 5:373–378, 2006.
- [7] C.A. Conti, E. Votta, A. Della Corte, L. Del Viscovo, C. Bancone, M. Cotrufo, and A. Redaelli. Dynamic finite element analysis of the aortic root from MRI-derived parameters. *Medical Engineering & Physics*, 32:212–221, 2010.

- [8] F.L. Xiong, W.A. Goetz, C.K. Chong, Y.L. Chua, S. Pfeifer, E. Wintermantel, and J.H. Yeo. Finite element investigation of stentless pericardial aortic valves: Relevance of leaflet geometry. *Annals of Biomedical Engineering*, 38:1908–1918, 2010.
- [9] F. Auricchio, M. Conti, S. Morganti, and P. Totaro. A computational tool to support pre-operative planning of stentless aortic valve prosthesis. *Medical Engineering & Physics*, 10.1016/j.medengphy.2011.05.006:–, 2011.
- [10] V. T. Nkomo, J. M. Gardin, T. N. Skelton, J. S. Gottdiener, C. G. Scott, and M. Enriquez-Sarano. Burden of valvular heart diseases: a population-based study. *The Lancet*, 368:1005–1011, 2006.
- [11] T.J.R. Hughes, A.J. Cottrell, and Y. Bazilevs. Isogeometric analysis: CAD, finite elements, NURBS, exact geometry, and mesh refinement. *Computer Methods in Applied Mechanics and Engineering*, 194:4135–4195, 2005.
- [12] J.A. Cottrell, T.J.R. Hughes, and Y. Bazilevs. *Isogeometric Analysis: Toward Integration of CAD and FEA*. John Wiley and sons, 2009.
- [13] J.A. Cottrell, T.J.R. Hughes, and A. Reali. Studies of refinement and continuity in isogeometric structural analysis. *Computer Methods in Applied Mechanics and Engineering*, 196:4160–4183, 2007.
- [14] Y. Bazilevs, V.M. Calo, J.A. Cottrell, J.A. Evans, T.J.R. Hughes, S. Lipton, M.A. Scott, and T.W. Sederberg. Isogeometric analysis using T-splines. *Computer Methods in Applied Mechanics and Engineering*, 199:229–263, 2010.
- [15] J.A. Cottrell, A. Reali, Y. Bazilevs, and T.J.R. Hughes. Isogeometric analysis of structural vibrations. *Computer Methods in Applied Mechanics and Engineering*, 195:5257–5296, 2006.
- [16] Y. Bazilevs, V.M. Calo, Y. Zhang, and T.J.R. Hughes. Isogeometric fluid-structure interaction analysis with applications to arterial blood flow. *Computational Mechanics*, 38:310–322, 2006.
- [17] T.J.R. Hughes, A. Reali, and G. Sangalli. Duality and unified analysis of discrete approximations in structural dynamics and wave propagation: comparison of  $p$ -method finite elements with  $k$ -method nurbs. *Computer Methods in Applied Mechanics and Engineering*, 197:4104–4124, 2008.
- [18] S. Lipton, J.A. Evans, Y. Bazilevs, T. Elguedj, and T.J.R. Hughes. Robustness of isogeometric structural discretizations under severe mesh distortion. *Computer Methods in Applied Mechanics and Engineering*, 199:357–373, 2010.
- [19] L. Piegl and W. Tiller. *The NURBS book. Monographs in visual communications*. Springer-Verlag, 1997.
- [20] K.S. Kunzelman, K.J. Grande, T.E. David, R.P. Cochran, and E.D. Verrier. Aortic root and valve relationships: impact on surgical repair. *Journal of Thoracic and Cardiovascular Surgery*, 107:162–170, 1994.

- [21] A. Rosset, L. Spadola, and O. Ratib. Osirix: An open-source software for navigating in multidimensional dicom images. *Journal of Digital Imaging*, 17:205–216, 2004.
- [22] D.J. Benson, Y. Bazilevs, M.-C. Hsu, and T.J.R. Hughes. Isogeometric shell analysis: the Reissner-Mindlin shell. *Computer Methods in Applied Mechanics and Engineering*, 199:276–289, 2010.
- [23] J. Kiendl, K.-U. Bletzinger, J. Linhard, and R. Wüchner. Isogeometric shell analysis with kirchhoff-love elements. *Computer Methods in Applied Mechanics and Engineering*, 198:3902–3914, 2009.
- [24] M.J. Thubrikar. *The Aortic Valve*. CRC Press, 1990.
- [25] J.-O. Hallquist. LS-DYNA theoretical manual. technical Report. Technical report, Livermore Software Technology Corporation, 1998.
- [26] D.R. Einstein, P. Reinhall, M. Nicosia, R.P. Cochran, and K. Kunzelman. Dynamic finite element implementation of nonlinear, anisotropic hyperelastic biological membranes. *Computer Methods in Biomechanics and Biomedical Engineering*, 6:33–44, 2003.
- [27] F. Saremi, S. Achenbach, E. Arbustini, and J. Narula. *Revisiting Cardiac Anatomy: a Computed-Tomography based Atlas and Reference*. Wiley-Blackwell, 2011.
- [28] W. Sun, A. Abad, and M.S. Sacks. Simulated bioprosthetic heart valve deformation under quasi-static loading. *Journal of Biomechanical Engineering*, 127:905–914, 2005.
- [29] H. Kim, J. Lu, M.S. Sacks, and K.B. Chandran. Dynamic simulation of bioprosthetic heart valves using a stress resultant shell model. *Annals of Biomedical Engineering*, 36:262–275, 2008.
- [30] K.J. Grande, R.P. Cochran, P.G. Reinhall, and K.S. Kunzelman. Stress variations in the human aortic root and valve: The role of anatomic asymmetry. *Annals of Biomedical Engineering*, 26:534–545, 1998.
- [31] F. Robicsek, M. J. Thubrikar, and A. A. Fokin. Cause of degenerative disease of the trileaflet aortic valve: review of subject and presentation of a new theory. *Annals of Thoracic Surgery*, 73:1346–1354, 2002.
- [32] T.J.R. Hughes, A. Reali, and G. Sangalli. Efficient quadrature for nurbs-based isogeometric analysis. *Computer Methods in Applied Mechanics and Engineering*, 199:301–313, 2010.
- [33] F. Auricchio, F. Calabrò, T.J.R. Hughes, A. Reali, and G. Sangalli. A simple algorithm for obtaining nearly optimal quadrature rules for nurbs-based isogeometric analysis. *Computer Methods in Applied Mechanics and Engineering*, 249-252:15–27, 2012.